Chinese Chemical Letters 32 (2021) 2463–2468

Contents lists available at ScienceDirect

Chinese Chemical Letters

journal homepage: www.elsevier.com/locate/cclet

Communication

Application of ion-in-conjugation molecules in resistive memories and gas sensors: The role of conjugation

Jialiang Wei[a], Jie Li[b], Chuang Yu[a], Qimeng Sun[a], Jinghui He[a,*], Jianmei Lu[a,*]

[a] College of Chemistry, Chemical Engineering and Materials Science, Collaborative Innovation Center of Suzhou Nano Science and Technology, National United Engineering Laboratory of Functionalized Environmental Adsorption Materials, Soochow University, Suzhou 215123, China
[b] Shanghai Institute of Measurement and Testing Technology, Shanghai 201203, China

ARTICLE INFO

Article history:
Received 29 December 2020
Received in revised form 3 March 2021
Accepted 7 March 2021
Available online 9 March 2021

Keywords:
Ion-in-conjugation
Organic electronic materials
RRAM
Gas sensing
Density functional theory

ABSTRACT

Ion-in-conjugation (IIC) materials are emerging as an important class of organic electronic materials with wide applications in energy storage, resistive memories and gas sensors. Many IIC materials were designed and investigated, however the role of conjugation in IIC materials' performance is yet investigated. Here we designed two molecules obtained by condensation of 4-butylaniline and oxocarbon acid. Squaric acid derivatives squaraine named SA-Bu and a croconamide named CA-Bu which only differ in their oxocarbon cores. While employing SA-Bu and CA-Bu as resistive memory and gas sensory materials, SA-Bu has attained promising performance in ternary memory and detection of NO_2 as low as 10 parts-per-billion whereas CA-Bu show mainly binary memory behavior and negligible NO_2 response. Theoretical calculations reveal that conjugation of CA-Bu was distorted by the increased steric hindrance, frustrating the charge transport and suppressing the conductivity. Our work demonstrates that the conjugation plays a crucial role in ion-in-materials promoting ternary RRAM devices and high-performance gas sensors manufacture.

In recent years, conjugated molecules with ionic fragments in their main chain were proposed for fabricating into various electronic devices chemical energy storage [1–3], resistance switching random access memory devices (RRAM) [4–6] and gas sensors [7–11]. These molecules were defined as the ion-in-conjugation (IIC) materials, such as derivatives of oxyallyl substructures like the squaraine [12–14], conjugated zwitterionic dyes [15,16], d-π-conjugated conductive coordination polymers [17–20]. The squaraine molecule/polymers are intensively utilized for chemiresistive sensing of trace-level gases molecules [21], achieving the lowest limit of detection (LOD) among all chemiresistive materials as well as environmental robustness [22]. Due to the ion-ion/ion-dipole attractions promoted by ionic groups located on the backbone, conjugated molecules with strong intermolecular forces are tend to approach to each other and crystallize easily. Additionally, owing to the introduction of zwitterionic resonating structures, IIC materials have high thermal, environmental and long-term stability.

On the other hand, the role of conjugation in the IIC materials for various applications has yet to be well understood. Particularly, the influence of conjugation on the performance of resistive memory and gas sensing is still unknown. This can be revealed by a comparative study of similar IIC molecules with finite discrepancy in its conjugated main chain. Therefore, in this work a squaraine molecule (noted as SA-Bu) and a new croconamide (noted as CA-Bu) were synthesized (Scheme 1) and their memory and gas sensing performances were studied. It is demonstrated that the SA-Bu-based devices mainly show ternary memory behavior whereas CA-Bu only show binary behaviors. More significantly, the sensory material CA-Bu only outputs negligible response to NO_2 whereas SA-Bu-based sensors exhibit satisfactory sensitivity and selectivity to NO_2. Structural and theoretical investigations on the croconamide and squaraine molecules reveal that the better sensing and ternary memory performance is attributable to the conjugation degree of these two molecules.

Preparation of two molecules: The squaraine molecule SA-Bu was synthesized as described in our previous work [23]. A mixture of squaric acid and 4-butylaniline in n-butanol/toluene (mixed with volume ratio of 1:1), stirred in reflux for 12 h. The afforded precipitate was filtered, rinsed with trichloromethane and hexane sequentially. ^{1}H NMR (400 MHz, DMSO-d_6): δ 9.79 (s, 2H), 7.39 (d, 4H, J = 8.4 Hz), 7.19 (d, 4H, J = 8.5 Hz), 2.55 (t, 4H, J = 7.6 Hz), 1.54 (t, 4H, J = 7.7 Hz), 1.34–1.27 (m, 4H), 0.90 (t, 6H, J = 7.3 Hz). The croconamide molecule CA-Bu was synthesized by adding

* Corresponding authors.
E-mail addresses: jinghhe@suda.edu.cn (J. He), lujm@suda.edu.cn (J. Lu).

https://doi.org/10.1016/j.cclet.2021.03.017

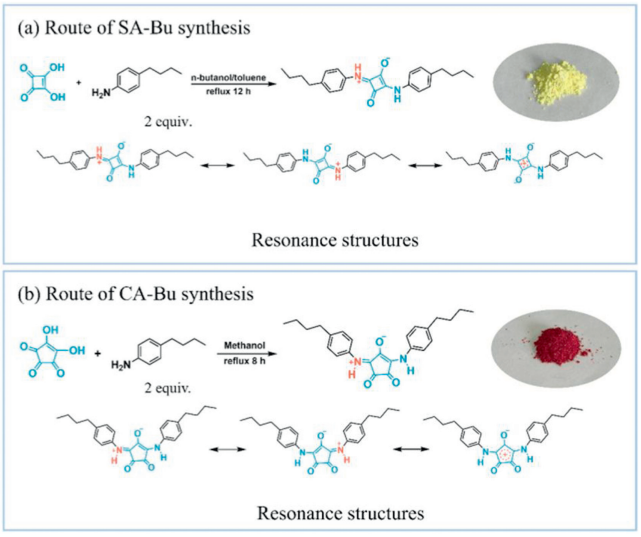

Scheme 1. Synthetic routes of SA-Bu and CA-Bu and their zwitterionic resonating structures.

4,5-dihydroxycyclopent-4-ene-1,2,3-trione (croconic acid) and 4-butyaniline (molar ratio 1:2) to methanol. After stirring for 8 h under reflux, the afforded precipitate was filtered, rinsed and dried in vacuum. ^{1}H NMR (400 MHz, DMSO-d_6): δ 11.48 (s, 2H), 7.34 (d, 4H, J = 8.0 Hz), 7.19 (d, 4H, J = 8.0 Hz), 2.59 (t, 4H, J = 7.7 Hz), 1.58 (q, 4H, J = 7.5 Hz), 1.32 (q, 4H, J = 7.4 Hz), 0.91 (t, 6H, J = 7.4 Hz). Squaric acid, croconic acid, 4-butylaniline, *n*-butanol, toluene and methanol were purchased from Tokyo Chemical Industry Ltd. (Japan) or Sinopharm Chemical Reagent Co., Ltd. (China). All chemical reagents used without further purification.

As shown in Fig. 1, the organic RRAM memory devices were prepared by thermal evaporation of SA-Bu and CA-Bu powder under high vacuum (10^{-6} Torr) onto indium tin oxide (ITO) coated glass substrates, by depositing the metallic aluminum electrodes, the electronic devices were obtained. To prepare chemiresistive gas sensors, the substrate was substituted by Ag/Pd interdigital electrode on a ceramic plate (electrode distance and channel width both 200 μm, overall dimension 14 × 7 × 0.64 mm) in the identical evaporation-deposition process. The fabricated sensors were used as gas sensors to detect nitric dioxide in subsequent experiments.

Materials characterization: ^{1}H NMR spectra were obtained on a Bruker Avance Neo 400 MHz FT-NMR spectrometer. Shimadzu UV-3600 spectrometer was used to obtain UV–vis absorption spectra. Used CorrTest CS Electrochemical Workstation analyzer to record cyclic voltammograms. The morphology of the synthesized materials was characterized by FE-SEM (Regulus 8230). Thermogravimetric analysis was performed on a Perkin-Elmer Diamond TG/DTA instrument under the protection of nitrogen gas with a heating rate of 10 °C/min. XRD measurement was performed with a Multiple Crystals X-ray Diffractometer (Bruker D8 Advance) using Cu Kα radiation (λ = 0.154 nm) at 30 kV and 40 mA in the 2θ region of 3°–40°.

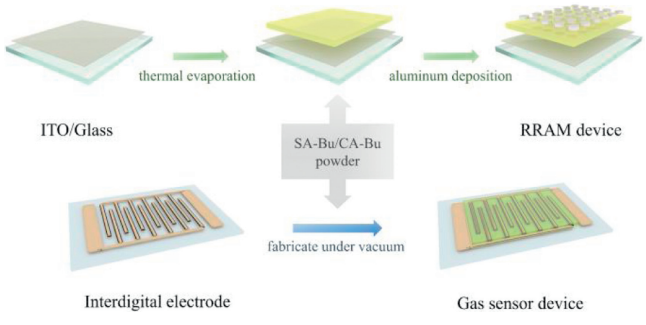

Fig. 1. Schematic diagram of the main steps to fabricate RRAM and gas sensor devices.

The ^{1}H NMR spectra confirm the product are successfully synthesized (Figs. S1 and S2 in Supporting information). The SEM images in Figs. S3 and S4 (Supporting information) show that SA-Bu powder is in the form of regular microrods with approximately 2–5 microns in length, while CA-Bu is crystalized in flat pallets with a similar dimension. Upon evaporation, the sizes of SA-Bu and CA-Bu grains in their film states are both smaller than that in their power state. Particularly, the grain size in the SA-Bu film is much smaller than that in the CA-Bu film, which is plausible to contribute the higher response of NO_2. The thermogravimetric analysis results (Fig. S5 in Supporting information) show that both the molecules remain stable at high temperatures (313 °C for SA-Bu and 274 °C for CA-Bu, when weight loss to 95% of the original), thus it is appropriate to use thermal evaporation to prepare devices. The X-ray diffraction pattern (XRD, Fig. S6 in Supporting information) of SA-Bu and CA-Bu thin films show prominent peak at $2\theta \approx 4.3°$, corresponding to around 21 Å interplanar spacing. This suggests the film formation of both the molecules on the ITO glass surface has experienced good crystallization. Two strong and sharp peaks initially observed in the powder state of SA-Bu disappeared, and replaced by a single prominent peak after forming the film. This can be attributed to preferential order induced by the presence of interface between film and substrate [24] as compared to the bulk powder which forms a 3D powder of micron-sized lamellar domains. All theoretical calculation performed based on density functional theory (DFT) were on a level of GGA-UBLYP/DNP implemented in DMol^3 code. Intermolecular interactions were semi-empirically corrected by Tkatchenko-Scheffler (TS) scheme. The converging criteria were set to a standard of 0.02 eV/Å in residue force and 1×10^{-5} eV in energy. Hirshfeld partitioned scheme was used to analyzed charge populations.

Performance measurement of fabricated devices: All electrical measurements of devices were performed on the Keithley 4200 SCS semiconductor parameter analyzer and Lakeshore robe station at a room temperature (25 °C). Specifically, the current-voltage (*I–V*) characteristics of the memory devices were measured by Keithley 4200 apparatus equipped with a pulse generator. The test was carried out in voltage sweep mode at ambient conditions. Besides, the gas sensing properties of the sensor devices was measured by placing the sensor in a sealed 1200 mL chamber and monitoring the change in current when the devices exposed to different concentrations of nitric dioxide. Humidity effect test was performed in an environment with a specified relative humidity condition obtained by separately adjusting flow rate of dry nitrogen and moist nitrogen after passing through a scrubber. The relative humidity (RH) in the air chamber is monitored by a commercial hygrometer. The relative response of sensors (R_s) was determined as the following equation:

$$R_s = \frac{\Delta I}{I_0} = (I - I_0)/I_0 \quad (1)$$

where I_0 is the stable current under pure nitrogen flow (flow rate 300 mL/min) and I denotes the real-time current.

Firstly, the memory behaviors were studied by the current-voltage curves of two typical electrical behaviors of SA-Bu-based devices and CA-Bu-based devices, respectively (Figs. 2a and b). These devices can switch to different resistance state during voltage sweep. When an external voltage from 0 V to −5 V was gradually applied to the SA-Bu-based memory device, two abrupt increases of current were observed at the switching threshold

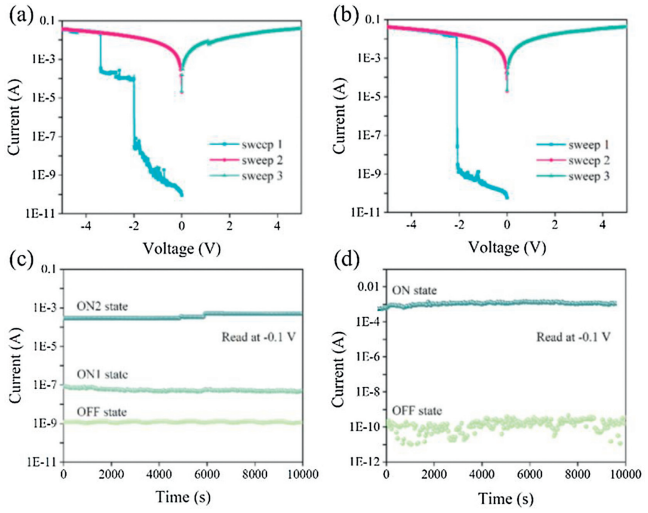

Fig. 2. (a) Typical ternary current-voltage characteristics of SA-Bu-based memory device. (b) The binary current-voltage characteristics of CA-Bu-based memory device. Stability tests of SA-Bu-based device under constant voltage stress at –0.1 V. Stability tests of memory devices under constant voltage stress at –0.1 V: (c) SA-Bu-based memory device; (d) CA-Bu-based device.

voltages of −1.96 and −3.38 V, forming three resistive states with a current ratio of $1:10^{2.63}:10^{5.41}$. These can be associated with the '0', '1', '2' states in the terms of ternary memory storage. In contrast, as shown in Fig. 2b, the CA-Bu-based RRAM devices behave only one abrupt jump of current state '0' and '1'. Therefore, the devices exhibit binary memory characteristics. Sweeps 2 and 3 were performed on the same cells for each types of all devices, indicating that neither negative bias nor positive bias could turn the device back to the poor conductive state. All multi-resistance states could be distinguished clearly and no significant degradation was observed after 10^4 s of continuous voltage bias at −0.1 V (Figs. 2c and d), suggesting a Write-Once-Read-Many Times (WORM) properties. Further statistics on a large sample size (120 samples) was conduct to check the reproducibility. The ternary device yield of the SA-Bu-based device is approximately 41%, consistent with the relevant yield mentioned in previous publication [23,24]. In contrast, the ternary yield of the CA-Bu-based device is only approximately 5% (Fig. S7 in Supporting information), which is far from satisfying for commercial application which means CA-Bu could not be used as a material capable of multilevel RRAM storage for the logic processing of complex information.

Subsequently, research on sensing performance of SA-Bu-base and CA-Bu-based gas sensors was first investigated by measuring transient response of these sensors toward N_2-diluted NO_2 gas at increasing concentrations from 10 ppb to 10 ppm as shown in Fig. 3a. A gradual increase in current can be observed for SA-Bu-based sensors. In contrast, sensors employed CA-Bu as sensory material possess a smaller background current level, and the corresponding current change induced by concentration variation is indiscernible ($<10^{-4}$ nA). Fig. 3b shows response and recovery performances of the SA-Bu-based sensor device. Taking the response at 100 ppb NO_2 as an example, the response time was 190 s. After NO_2 off, the current returned to 90% of the initial level within 171 s under pure N_2 purging. The current-voltage characteristics (Fig. 3c) indicated when the as-fabricated sensor device exposed to N_2-diluted NO_2 gas, the current grows linearly with the increase in voltage. To determine the selectivity performance of SA-Bu-based sensor, it was exposed to various inorganic gases and 10 ppm organic vapors (Fig. 3d). Although NO has the second largest response, its sensitivity is 33-flod less than that of NO_2, causing insignificant interference in NO_2 detection. This selectivity result is gratifying as to ensure the devices to maintain the ability to distinguish gases in a complex atmosphere. In addition, these SA-Bu-based sensors perform reliable and good batch-to-batch reproducible response, good repeatability and long-term stability even after being worked over one month (Figs. 3e and f).

The response of SA-Bu-based sensors to NO_2 under different RH ambientes is shown in Fig. 4. Notably, the base current of SA-Bu-based sensor in clean N_2 is significantly increased under constant voltage as the ambient becomes damp. This could be associated with a sequence of proton-transfer process dominated by the Grotthuss mechanism [25–27] in which H^+ or H_3O^+ species hop

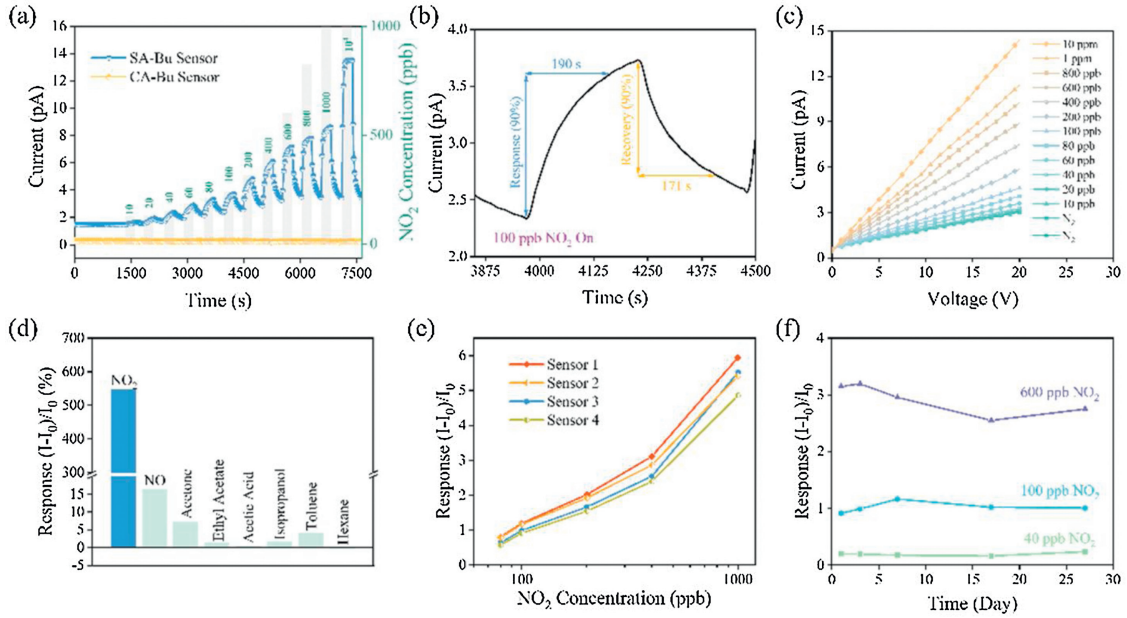

Fig. 3. (a) Transient responses with increasing NO_2 concentrations at the ppb level of sensors employed SA-Bu and CA-Bu. (b) Response/recovery time to 100 ppb NO_2. (c) Current-voltage characteristics of SA-Bu-based sensor exposed to the gas flow with NO_2 concentrations ranging from 10 ppb to 10 ppm. (d) Selectivity.

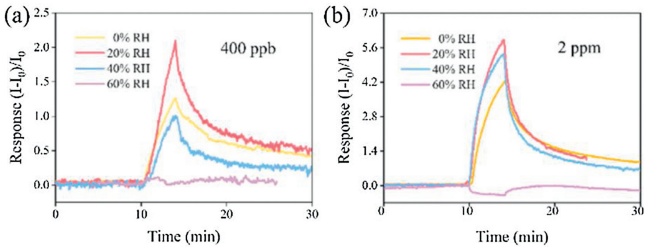

Fig. 4. Response to exposure to NO_2 at different concentrations under different RH atmospheres, room temperature. (a) 400 ppb NO_2. (b) 2 ppm NO_2.

among the hydrogen-bonded water molecules. In addition, as the RH increases, the basic current affected by ambient water molecules and the transient current exposure to NO_2 have different current trends. Our previous work has confirmed the adsorption of water molecules and NO_2 molecules is a competitive phenomenon. NO_2 has higher affinity compared to water molecules, but competes with water molecules hinders the adsorption of NO_2 [21] (More details of the trend comparison, see Fig. S8 in Supporting information). As the RH increases to 60%, water molecules contribute more to the current increase, making the NO_2 response signal quite low. For RH > 60%, it is impossible to evaluate the response and the sensitivity of NO_2 concentrations. The investigation on the relationship between the response and the RH found that the SA-Bu-based sensor maintains the ability to detect low concentrations of NO_2 under 40% RH, which can suffice the needs of practical applications under low and medium relative humidity conditions at a room temperature.

Compared to other NO_2 sensors recently reported in Table 1 [28–36], the SA-Bu-based gas sensor in this work has advantages in terms of low limit of detection, high NO_2 sensitivity and operation ability at room temperature.

To understand why CA-Bu and SA-Bu have distinct performance in memory and gas sensing, the latter showed an overwhelming advantage, we firstly consider their discrepancies in film conductance. In the memory devices, the conductance nonlinear hopping under different voltages, while in the gas sensors the conductivity response to the external gas atmosphere. Both SA-Bu and CA-Bu active films deposited on the original ITO glass show high quality with smooth surface (relatively small root-mean-square surface roughness = 1.05 and 0.60 nm, respectively, morphology measured by atomic force microscopy, Figs. S9a and b in Supporting information) due to good crystallinity of these two materials. The thickness of the deposited molecular film is approximately 150 nm (determined by AFM, Figs. S9c and d in Supporting information), and the thickness of deposited aluminum is controlled at approximately 100 nm. Given the same film quality and thickness, the device performance discrepancies are attributable to the film conductance. The conductivity flowing between the electrodes can be written as a product between carrier density, carrier mobility and effective electric field [37]:

$$G = N \times E \times \mu \quad (2)$$

where N is the carrier density, E is the effective electric field and μ is the carrier mobility, respectively.

We first survey the divergences in the carrier density N. Pristine SA-Bu and CA-Bu are provided with optical gap of 2.76 eV and 1.89 eV estimated from its UV–vis spectrum (Fig. S10 in Supporting information). The HOMO-LUMO energy levels are obtained through calculations and spatial plots of the molecular orbitals are presented in Fig. S11 (Supporting information). The figure shows that the distribution density of SA-Bu and CA-Bu are similar. The calculated HOMO-LUMO gaps are 2.20 eV and 1.57 eV for SA-Bu and CA-Bu, respectively, which is of similar trend to the UV–vis result. In this term, CA-Bu ought to have lower band gaps and in consequence higher intrinsic carrier density N under the same thermal condition [38–40], which cannot explain the poorer conductivity of CA-Bu.

In the case of gas sensors, N will sharply rise due to contribution from doped carriers when nitric dioxide interaction with our p-type sensory materials SA-Bu and CA-Bu. We performed calculated charge analysis predicting the binding mode between sensory molecules and NO_2 (Fig. S9). The interaction model of SA-Bu molecule and NO_2 with hydrogen bonds seems to be the most stable model, which produces the greatest binding energy of 0.38 eV and 0.038 electrons transferred from SA-Bu molecule to NO_2. The interaction model of SA-Bu molecule and NO_2 also offer approachable binding energy (0.21, 0.26 and 0.23 eV) and electron transfer (0.114, 0.077 and 0.080 e^-). Thus, the doping carrier density offered by NO_2 doping in both films should be comparable. To sum up, the large difference in the conductivity at low electric field of memory or low NO_2 gas concentration in sensing, should not stem from the difference in carrier density, neither in the case of memory nor sensors.

Next, we consider the role of effective electric field. The electric field intensity E that drives the charge transport also affects the current flowing of organic electronic materials. A mechanism we previously reported is related to this factor [24], which could conductive channels triggers the first current level step from the

Table 1
Comparison of some recent reported sensory materials for NO_2 detection.

Material	Temperature (°C)	Limit of detection	Sensitivity[a]	Reference
Graphene	r.t.	1 ppm	0.1	[28]
SnO_2/graphene	150	1 ppm	24.7	[29]
MoS_2	r.t.	100 ppm	0.3	[30]
PbS/MoS_2	r.t.	200 ppb	1.23	[31]
WO_3	300	500 ppb	8	[32]
CoPc	115	1 ppm	0.25	[33]
FeHNPs-PANI	r.t.	570 ppb	0.23	[34]
TPCAs	r.t.	190 ppb	—	[35]
Pentacene	r.t.	100 ppb	0.3	[36]
SA-Bu	r.t.	10 ppb	5.5	This work

[a] Sensitivity are calculated based on the following equation: Sensitivity $= \frac{\text{Response}}{\text{Concentration (ppm)}}$

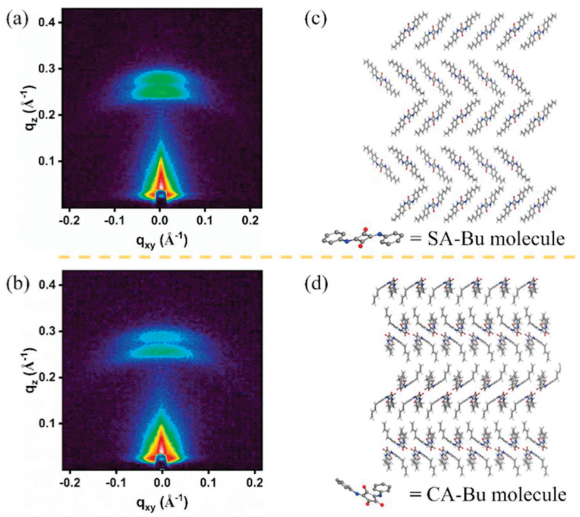

Fig. 5. GISAXS patterns of (a) SA-Bu and (b) CA-Bu. (c, d) Schematic diagrams of possible stacking manners, molecular models shown in the figure omit the alkyl chains.

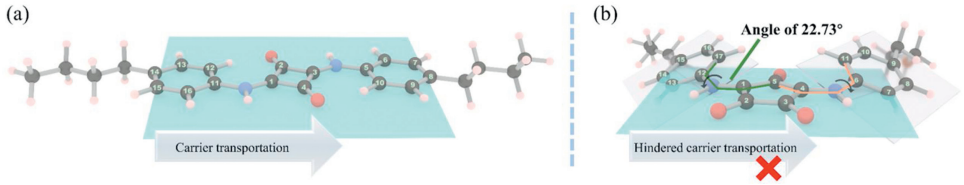

Fig. 6. Molecular structures geometric optimized by DFT calculation of (a) SA-Bu and (b) CA-Bu, with two dihedral angles.

OFF to ON1 state of organic RRAM memory devices. The higher external bias applied, the conductive channels grow wider and the quantum conductance disappears driven by electric field, resulting in switching from ON1 to ON2 state. Organic layers consist of SA-Bu and CA-Bu molecule materials play a role of the matrix for holding the top electrode and act as diodes to regulate the external voltage to trigger quantized conductance. The extra voltage (ΔV) consumed is inevitable to overcome the obstacles encountered during the directional migration of electrons, those troubles may be caused by the interfaces and grain boundaries of organic molecules. On the other hand, the effective electric field E in terms of voltage loss, is expected to be the same during gas sensing. While a certain external voltage was applied to the two electrodes, the effective voltage applied to the organic crystalline is generally smaller, as part of voltage will loss at the grain boundaries [41].We recorded the grazing-incidence small-angle X-ray scattering spectra (GISAXS, Fig. 5) to further illustrate the stacking manners of SA-Bu and CA-Bu in the film. The films deposited on ITO glass of both materials can clearly find two arcs in the q_z direction, which shows that they have a highly ordered planar outer layer structure. For SA-Bu, its two arcs are centered at q_z = 0.277 Å and 0.261 Å, corresponding to d = 22.7 Å and 24.1 Å (calculated from $d = 2\pi/q_z$). Notably, two arcs similar to SA-Bu arcs twin brothers can be found in the pattern of the CA-Bu film whose q_z = 0.289 Å and 0.275 Å, corresponding to d = 21.7 Å and 22.8 Å. Both SA-Bu and CA-Bu molecules are composed of rigid cores and two flexible terminal alkyl chains. Two arcs reflect parallel lamellae structures with cores stack *via* $\pi-\pi$ stacking and alkyl chains between adjacent layers attracting each other. The highly similar GISAXS images imply similar surface morphology and crystallite orientation preference [42,43]. Both molecules have quite good crystallization property, which may be a property shared by ion-in-conjugation materials. Herein, the possible stacking manners of SA-Bu and CA-Bu are proposed in Figs. 5c and d, based on the same crystalline orientation and common organic molecular packings seen in the existing literature [44,45]. With the above two factors being excluded, only the carrier mobility μ difference in SA-Bu and CA-Bu film are responsible for the memory and sensing performances. Molecules have different charge transportation capabilities, since organic molecules are considered to be effective electrical transmissions when they are connected by a relatively planar [46]. After geometric optimization, the computed molecular structures are displayed in Fig. 6. Ignoring the loose terminal alkyl chains, SA-Bu molecule has a rigid conjugated center, with its squaric ring and two phenyl rings completely situated in the same plane. On the contrary, CA-Bu has a completely different molecular non-planar structure. There are two obvious dihedral angles of 22.73° ($C_5-C_1C_{12}-C_{17}$) and 24.10° ($C_5-C_4C_6-C_{11}$) between the croconic plane and the phenyl rings because of steric crowding preventing planar configurations. Distortions caused the decrease of degree of conjugation and the molecular structure is not conducive to charge transport, resulting in a lower charge mobility [47–49]. Although the performance of organic electronic devices is governed by many factors, not only the suitable circumstances for charge transport, but the high carrier transportation mobility tends to increase current density and reduce power consumption and plays the role as internal element of the structure-performance relationships. Fig. 7 schematically illustrate the proposed mechanisms mentioned above.

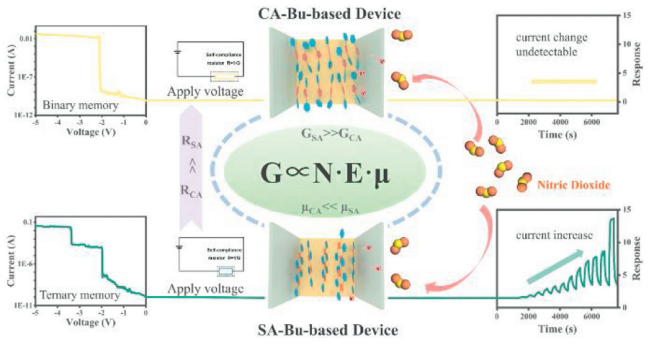

Fig. 7. Proposed mechanism diagram.

In conclusion, SA-Bu is demonstrated feasible for ternary memory storage and it shows a promising capability for detecting NO_2, limit of detection as low as 10 ppb benefited from its perfect conjugation. In contrast, since the conjugate planes of CA-Bu was distorted by the increased steric hindrance, frustrated charge transport barriers forms, leading a violent decline in device conductance. Although croconamide has strong interaction with both neighboring molecules and external gas molecules due to its zwitterionic properties, to utilize croconic acid (CA) as organic electronic materials, its conductivity needs to improve by external stimuli such as light or heat. Through comparative research from structure-performance relationships to performances in distinct scenarios, our work demonstrates that the conjugation plays an essential role in ion-in-materials promoting ternary RRAM devices and high-performance gas sensors manufacture.

Declaration of competing interest

The authors declare that they have no known competing financial interests or personal relationships that could have appeared to influence the work reported in this paper.

Acknowledgments

We gratefully acknowledge the financial support provided by the National Key R&D Program of China (Nos. 2020YFC1818401, 2017YFC0210906), National Natural Science Foundation of China (Nos. 21978185, 21938006, 21776190), Basic Research Project of Leading Technology in Jiangsu Province (No. BK20202012), Suzhou Science and Technology Bureau Project (No. SYG201935) and the project supported by the Priority Academic Program Development of Jiangsu Higher Education Institutions (PAPD).

Appendix A. Supplementary data

Supplementary material related to this article can be found, in the online version, at doi:https://doi.org/10.1016/j.cclet.2021.03.017.

References

[1] F. Xu, S.H. Yang, X. Chen, et al., Chem. Sci. 10 (2019) 6001–6006.
[2] C. Risko, M.D. McGehee, J.L. Brédas, Chem. Sci. 2 (2011) 1200–1218.
[3] X. Wu, B. Huang, Q. Wang, et al., Chem. Eng. J. 373 (2019) 493–500.
[4] X.F. Cheng, X. Hou, W.H. Qian, et al., ACS Appl. Mater. Interfaces 9 (2017) 27847–27852.
[5] Y. Cao, X. Tian, J. Gu, et al., Angew. Chem. Int. Ed. 57 (2018) 4543–4548.
[6] Y.Y. Zhao, W.J. Sun, J.H. He, et al., Adv. Electron. Mater. 5 (2019) 1800964.
[7] S. Carquigny, J.B. Sanchez, F. Berger, et al., Talanta 78 (2009) 199–206.
[8] M.G. Guillén, F. Gámez, T. Lopes-Costa, et al., Sens. Actuators B: Chem. 236 (2016) 136–143.
[9] C.F. Lu, C.W. Shih, C.A. Chen, et al., Adv. Funct. Mater. 28 (2018) 1803145.
[10] M. Ganiga, J. Cyriac, Sens. Actuator. B: Chem. 225 (2016) 522–528.
[11] J. Zhou, X.F. Cheng, B.J. Gao, et al., Small 15 (2019) e1803896.
[12] K. Yesudas, K. Bhanuprakash, J. Phys. Chem. A 111 (2007) 1943–1952.
[13] C.B. Larsen, J.E. Barnsley, H. van der Salm, et al., Eur. J. Org. Chem. 2017 (2017) 2432–2440.
[14] X. Xiao, Q.J. Zhang, J.H. He, et al., Sens. Actuators B: Chem. 255 (2018) 1147–1152.
[15] A. Ajayaghosh, C.R. Chenthamarakshan, S. Das, et al., Chem. Mater. 9 (1997) 644–646.
[16] J. Wang, X.F. Cheng, W.H. Qian, et al., J. Mater. Chem. C 8 (2020) 7658–7662.
[17] G. Givaja, P. Amo-Ochoa, C.J. Gomez-Garcia, et al., Chem. Soc. Rev. 41 (2012) 115–147.
[18] X.F. Cheng, E.B. Shi, X. Hou, et al., Adv. Electron. Mater. 3 (2017) 1700107.
[19] Y. Wu, Y. Chen, M. Tang, et al., Chem. Commun. 55 (2019) 10856–10859.
[20] X.F. Cheng, J. Li, X. Hou, et al., Sci. China Chem. 62 (2019) 753–760.
[21] C. Yu, H.Z. Lin, J. Zhou, et al., J. Mater. Chem. A 8 (2020) 1052–1058.
[22] X. Xiao, X.F. Cheng, X. Hou, et al., Small 13 (2017) 1602190.
[23] X. Hou, X. Xiao, Q.H. Zhou, et al., Chem. Sci. 8 (2017) 2344–2351.
[24] X.F. Cheng, Y. Zhao, W. Ye, et al., J. Mater. Chem. C 8 (2020) 2964–2969.
[25] N. Agmon, Chem. Phys. Lett. 244 (1995) 456–462.
[26] X. Qian, L. Chen, L. Yin, et al., Science 370 (2020) 596–600.
[27] W. Yan, M.A. Worsley, T. Pham, et al., Appl. Surf. Sci. 450 (2018) 372–379.
[28] Y. Seekaew, D. Phokharatkul, A. Wisitsoraat, et al., Appl. Surf. Sci. 404 (2017) 357–363.
[29] H.W. Kim, H.G. Na, Y.J. Kwon, et al., ACS Appl. Mater. Interfaces 9 (2017) 31667–31682.
[30] X. Yu, D. Wang, Y. Wang, et al., Chin. Chem. Lett. 31 (2020) 2099–2102.
[31] J. Tan, J. Hu, J. Ren, et al., Chin. Chem. Lett. 31 (2020) 2103–2108.
[32] Z. Hua, C. Tian, Z. Qiu, et al., Sens. Actuator. B: Chem. 259 (2018) 250–257.
[33] Q. Liu, L. Gao, X. Su, et al., Mater. Chem. Phys. 234 (2019) 94–101.
[34] S.G. Kim, J. Jun, J.S. Lee, et al., J. Mater. Chem. A 7 (2019) 8451–8459.
[35] H. Chae, S. Hwang, J.E. Kwon, et al., Dye. Pigments 186 (2021) 109017.
[36] M. Mirza, J. Wang, L. Wang, et al., Org. Electron. 24 (2015) 96–100.
[37] J.C. Scott, L.D. Bozano, Adv. Mater. 19 (2007) 1452–1463.
[38] N. Santhanamoorthi, C.M. Lo, J.C. Jiang, J. Phys. Chem. Lett. 4 (2013) 524–530.
[39] S. Zhang, M. Xie, F. Li, et al., Angew. Chem. Int. Ed. 55 (2016) 1666–1669.
[40] E.M.J. Hedegaard, S. Johnsen, L. Bjerg, et al., Chem. Mater. 26 (2014) 4992–4997.
[41] D. Qian, Z. Zheng, H. Yao, et al., Nat. Mater. 17 (2018) 703–709.
[42] Y.F. Huang, C.W. Chang, D.M. Smilgies, et al., Adv. Mater. 21 (2009) 2988–2992.
[43] F. Huang, P. Siffalovic, B. Li, et al., Chem. Eng. J. 394 (2020) 124959.
[44] B. Park, K. Kim, J. Park, et al., ACS Appl. Mater. Interfaces 9 (2017) 27839–27846.
[45] H. Jiang, P. Hu, J. Ye, et al., Angew. Chem. Int. Ed. 57 (2018) 8875–8880.
[46] A. Kokil, I. Shiyanovskaya, K.D. Singer, et al., J. Am. Chem. Soc. 124 (2002) 9978–9979.
[47] H. Lin, S. Chen, H. Hu, et al., Adv. Mater. 28 (2016) 8546–8551.
[48] Y. Watanabe, R. Yoshioka, H. Sasabe, et al., J. Mater. Chem. C 4 (2016) 8980–8988.
[49] S. Fratini, M. Nikolka, A. Salleo, et al., Nat. Mater. 19 (2020) 491–502.